

NMR structure of a lytic polysaccharide monooxygenase provides insight into copper-binding, protein dynamics and substrate interactions

Finn L. Aachmann^{a,1}, Morten Sørli^b, Gudmund Skjåk-Bræk^a, Vincent G. H. Eijsink^b, Gustav Vaaje-Kolstad^{b,1}

^aDepartment of Biotechnology, NOBIOPOL, Norwegian University of Science and Technology, N-7491 Trondheim, Norway; ^bDepartment of Chemistry, Biotechnology and Food Science, Norwegian University of Life Sciences P.O. Box 5003, NO-1432 Aas, Norway

Classification: Biological sciences, biochemistry.

Author contributions: FLA, GVK, MS, GSB and VGHE designed research; FLA, GVK and MS performed research; FLA, GVK, MS, GSB and VGHE analyzed data; and FLA, GVK, MS and VGHE wrote the paper.

Abbreviations and acronyms: aa: amino acid, CBP21_{apo}: metal free CBP21, HSQC: heteronuclear single quantum coherence, ITC: isothermal titration calorimetry, LPMO: lytic polysaccharide monooxygenase, NMR: nuclear magnetic resonance spectroscopy, PRE: paramagnetic relaxation enhancement, *TaGH61A*: *Thermoascus aurantiacus* GH61A, TMP: *N,N,N',N'*-tetramethyl-1,4-phenylenediamine.

Keywords: lytic polysaccharide monooxygenase, GH61, CBM33, polysaccharide monooxygenase, chitin

¹To whom correspondence may be addressed. Finn L. Aachmann Tel.: +4773593317, Address: Department of Biotechnology, NOBIOPOL, Norwegian University of Science and Technology, N-7491 Trondheim, Norway, E-mail: finn.aachmann@biotech.ntnu.no or Gustav Vaaje-Kolstad Tel.: +47 64965905 Address: Department of Chemistry, Biotechnology and Food Science Norwegian University of Life Sciences P.O. Box 5003, NO-1432 Aas, Norway, Email: gustav.vaaje-kolstad@umb.no.

Abstract

Lytic polysaccharide monooxygenases currently classified in the CBM33 and GH61 families of carbohydrate-active enzymes are likely to play important roles in future biorefining. Still, the molecular basis of their unprecedented catalytic activity remains largely unknown. We have used NMR techniques and isothermal titration calorimetry (ITC) to address structural and functional aspects of CBP21, a chitin-active CBM33. NMR structural and relaxation studies showed that CBP21 is a compact and rigid molecule, the only exception being the catalytic metal-binding site. ^{15}N and ^{13}C HSQC spectra showed that His28 and His114 in the catalytic center bind a variety of divalent metal ions with a clear preference for Cu^{2+} ($K_d = 55$ nM; from ITC) and even more so Cu^{1+} ($K_d \approx 1$ nM; this value was derived from an experimentally determined redox potential for CBP21- Cu^{2+} of 275 mV using a thermodynamic cycle). Strong binding of Cu^{1+} was also reflected in a reduction in the $\text{p}K_a$ values of the histidines by 3.6 and 2.2 pH units, respectively. Cyanide, a mimic of molecular oxygen, was found to bind to the metal ion only. These data support a model where copper is reduced on the enzyme by an externally provided electron, followed by oxygen binding and activation by internal electron transfer. Interactions of CBP21 with a crystalline substrate were mapped in a $^2\text{H}/^1\text{H}$ exchange experiment, which showed that substrate binding involves an extended planar binding surface, including the metal binding site. Such a planar catalytic surface seems well suited to interact with crystalline substrates.

/body

Introduction

Chitin and cellulose represent some of nature's largest reservoirs of organic carbon in the form of monomeric hexose sugars (*N*-acetyl-glucosamine and glucose, respectively) linearly linked by β -1,4 glycosidic bonds. In their natural form, both polysaccharides are organized in crystalline arrangements that make up robust biological structures, like crustacean cuticles (chitin) or plant cell walls (cellulose). While this crystalline nature is crucial for biological function it provides a tough challenge in industrial biorefining of biomass, where efficient enzymatic depolymerization of particularly cellulose is a critical step.

Enzymatic degradation of recalcitrant polysaccharides has traditionally been thought to occur through the synergistic action of hydrolytic enzymes that have complementary activities (1, 2). Endo-acting hydrolases make random scissions on the polysaccharide chains, while exo-acting processive hydrolases mainly target chain ends. However, during the last two years, a new enzyme family targeting recalcitrant polysaccharides has been identified, namely the lytic polysaccharide monooxygenases (LPMOs; also referred to as lytic polysaccharide oxidases (3), polysaccharide monooxygenases (4) and oxidohydrolases (5)). In contrast to the classic hydrolytic enzymes that comprise many enzyme families, LPMOs only group into two distinct families (6), carbohydrate binding module family 33 (CBM33), with bacterial, viral and some eukaryotic members and glycoside hydrolase family 61 (GH61), with so far only fungal members. The two LPMO families share a common fold, with a flat substrate binding surface that contains a metal-binding site including two conserved histidines ((5, 7, 8); see below).

LPMO activity was first documented for CBP21, a CBM33 secreted by the chitinolytic bacterium *Serratia marcescens*, which previously had been shown to boost chitin depolymerization by chitinases (9). CBP21 catalyzes oxidative cleavage of the β -1,4 glycosidic bonds that results in oxidation of the C1 carbon (5). The reaction involves molecular oxygen, an external electron donor and a metal that is coordinated by the two conserved histidines (Fig. 1). The identity of the metal was not disclosed in early work (5, 10) but functional studies on related enzymes, a CBM33 from *Enterococcus faecalis* (11) and three GH61s (4, 12, 13), have later indicated that the LPMOs are copper dependent enzymes. Still, due the several complications, such as the indiscriminate nature of the metal binding site (see below) and the fact that CBM33 crystal structures obtained so far mostly were metal-free, many aspects of metal-binding remain unresolved. Even less is known about how these enzymes, with their unique flat binding surfaces devoid of traditional substrate-binding "grooves" or "pockets", interact with the substrate. Nothing is known about dynamics in these remarkably compact proteins.

Here we describe the solution structure of CBP21 determined by nuclear magnetic resonance spectroscopy (NMR). Both NMR and isothermal titration calorimetry (ITC) were used to investigate metal binding and its pH dependence. Furthermore, we studied the molecular basis of cyanide inhibition as well as protein dynamics. Finally, by applying an NMR based approach that exploits the pH dependency of substrate binding we were able to directly map the substrate-binding surface of CBP21. Thus, we provide

important insights into fundamental properties underlying the unprecedented and unresolved catalytic mechanism of these recently discovered enzymes.

Results

CBP21 structure. The solution structure of CBP21 (Fig. 1A and Table S1; deposited in the PDB with ID 2LHS) was calculated based on 4330 NOE-derived geometrical constraints, 231 TALOS+ (14) derived dihedral angles restraints and two disulphide bridges (8), Cys41-Cys49 and Cys135-Cys162. The CBP21 core structure is formed by a distorted β -sandwich consisting of nine anti-parallel and one parallel β -strands. The exterior of the protein is decorated with one short α -helix, four short $^3_{10}$ -helix segments and several ordered loops. Fig. 1A shows that the solution structure of CBP21 is highly similar to the X-ray crystallographic structure (8); there are, however minor differences in a solvent exposed area of the enzyme that is involved in substrate-binding (discussed below).

Metal binding. Interaction of CBP21 with divalent metals was probed by recording changes in chemical shifts in ^{15}N HSQC spectra during titration with Ca^{2+} , Mg^{2+} , Fe^{3+} , Co^{2+} , Zn^{2+} or Cu^{2+} ions (Figs. 1B, 1C and S1). All ions showed binding to an interaction site located between His28 and His114, where the side-chains of both residues and the N-terminal amino group of His28 coordinate the metal ion (Fig. 1D; it should be noted that the N-terminal leader peptide is taken into account when numbering the amino acids of CBP21; His28 is the N-terminal residue of the mature protein). Based on these experiments the dissociation constants (K_d) for the various metals were estimated to have the following order: $\text{Ca}^{2+} > \text{Mg}^{2+} > \text{Fe}^{3+} > \text{Co}^{2+} \gg \text{Zn}^{2+} > \text{Cu}^{2+}$, varying from > 10 mM for Ca^{2+} to < 0.5 mM for Co^{2+} and substantially lower for Zn^{2+} and Cu^{2+} (Fig. S1).

Considering the involvement of histidines in metal binding, ^{13}C HSQC spectra of the aromatic region were recorded in the absence and presence of Zn^{2+} , Cu^{2+} or Cu^{1+} . For Zn^{2+} titration, new peaks for His28 and His114 coordinating Zn^{2+} appeared and increased in intensity upon titration (Fig. 2A). The titrations showed strong binding of Zn^{2+} and indicated a K_d in a concentration range (low micromolar) that is too low for determination by NMR. Obtaining K_d values for the binding of Cu^{2+} was impossible because of the paramagnetic properties of Cu^{2+} that lead to broadening of the NMR signals of residues within $\sim 10\text{\AA}$ from the copper binding site to levels beyond detection (see also (15)). However, a competition experiment clearly showed that Cu^{2+} binds more tightly than Zn^{2+} (Fig. 2B). Upon titration of metal-free CBP21 with Cu^{2+} , the signal for both histidines disappeared already at a 1:1 molar ratio between protein and the metal ion (Fig. 2D). Competition experiments also showed that Cu^{1+} binds more strongly than Zn^{2+} (Fig. 2C) and Cu^{2+} (Fig. 2E).

Since the K_d values were too low to be precisely determined from the NMR data, ITC experiments were conducted to obtain more accurate data. Due to the low solubility of Cu^{1+} , only dissociation constants for Zn^{2+} and Cu^{2+} were determined, at 330 nM and 55 nM, respectively (Table 1 and Fig. 3). In agreement with the NMR data, this showed that CBP21 had higher affinity for Cu^{2+} than for Zn^{2+} (6-fold). The K_d for Cu^{1+} binding can be obtained by combining, in a thermodynamic cycle, the energetics of Cu^{2+} dissociation from CBP21 and the electron transfer reaction between aqueous Cu^{2+} and CBP21- Cu^{1+} (Fig. S2). The latter was obtained by experimentally determining the equilibrium constant between CBP21- Cu^{2+} and a suitable electron transfer mediator (TMP, see (16)). The E° for the equilibrium: $\text{TMP}_{\text{red}} + \text{CBP21-Cu}^{2+} \rightleftharpoons \text{TMP}_{\text{ox}} + \text{CBP21-}$

Cu^{1+} was determined to be 2 mV (Fig. S2, I). Subtraction of the E° for the $\text{TMP}_{\text{ox}}/\text{TMP}_{\text{red}}$ redox couple yields an E° of 275 mV for the CBP21-Cu(II)/CBP21-Cu(I) redox couple, a value that is 115 mV higher than that of aqueous $\text{Cu}^{2+}/\text{Cu}^{1+}$ (Fig. S2, II). Since the values are related according to the thermodynamic cycle depicted in Fig. S2, the 115 mV increase in redox potential reflects tighter binding of Cu^{1+} relative to Cu^{2+} and leads to a calculated K_d for Cu^{1+} of 1.2 nM (Fig. S2, III). Notably, this value should be considered an estimate, particularly because the thermodynamic values used in the cycle due to technical limitations had to be determined at slightly different temperatures (varying from 6 °C to 25 °C).

To illustrate the functional implications of these findings, and exploiting a novel method for generating metal-free CBP21 (CBP21_{apo}; by reduction in pH, see below), we examined the enzymatic activity of CBP21_{apo} in the presence of a metal chelator (EDTA) and various added metal ions. The data clearly show that Cu^{2+} is the only of the tested divalent metals that is able to reactivate metal-free (and completely inactive) CBP21_{apo} (Fig. 4 and S3).

Cyanide inhibition. Cyanide inhibits CBP21 (5), most likely because it is a dioxygen mimic. Addition of sodium cyanide to CBP21- Zn^{2+} resulted in substantial chemical shifts for His28 and His114 in both ^{15}N and ^{13}C HSQC NMR spectra (Fig. S4), whereas only limited changes were observed for other residues.* In a control experiment where CBP21_{apo} was incubated with cyanide, no changes were observed for either the ^{15}N or ^{13}C HSQC NMR spectra, indicating that the effect of cyanide is highly local, as would be the case if this oxygen mimic binds directly to the metal ion.

pH-titrations. By acid titration of CBP21_{apo} the $\text{p}K_a$ values of His28 and His114 were determined to be 7.03 ± 0.25 and 5.85 ± 0.09 , respectively (Fig. 5A,B), which are common values for histidines in proteins (17). In the presence of Zn^{2+} , both histidine residues first started to titrate below pH 5.0 and were fully protonated at pH 4.0 (Fig. 5C). The degree of protonation was calculated based on the integrals for the His- Zn^{2+} and His- H^+ peaks and this indicated that both histidines have a $\text{p}K_a$ between 4.3-4.4. Both histidines first started to exchange Cu^{1+} with protons below pH 4.7 and were fully protonated first at pH 2.9 (Fig. 5D), with $\text{p}K_a$ values of 3.3-3.5 and 3.5-3.7 for His28 and His114, respectively.

Altogether, the $\text{p}K_a$ perturbations of the histidines by the metal ions clearly show that Cu^{1+} binds stronger than Zn^{2+} , and that the enzyme is in its apo-form at $\text{pH} < 2.9$.

The variation in $\text{p}K_a$ perturbations will to a certain extent reflect the difference in binding strength of Cu^{1+} vs. Zn^{2+} and this may be used to estimate the K_d for Cu^{1+} . The observed differences in the $\text{p}K_a$ perturbations exerted by Cu^{1+} compared to Zn^{2+} correspond to a total free energy change (ΔG_r°) of 2.3 kcal/mol, 1.0 kcal/mol for His28 and 1.3 kcal/mol for His114 (calculated by using $\Delta G_r^\circ = -RT \ln K$). Adding this free energy change to the free energy change of Zn^{2+} binding (8.3 kcal/mol, from ITC data, Table 1) yields a ΔG_r° of 10.6 kcal/mol, corresponding to a K_d of 16 nM. This calculation is based on the rather unlikely assumption that 100 % of the binding free energy is reflected in the measured $\text{p}K_a$ values and, thus, the value of 16 nM represents

* Due to the paramagnetic properties of Cu^{2+} (not visible in NMR experiments) and the experimental challenges in working with Cu^{1+} (low solubility), Zn^{2+} was chosen as the metal ligand.

an upper limit, rather than the real value. The upper limit of 16 nM for the K_d for Cu^{1+} is lower than the K_d for Cu^{2+} determined with ITC (55 nM) and is compatible with the K_d value for Cu^{1+} obtained using the thermodynamic cycle described above (1.2 nM).

Mobility studies. The CPB21 metal binding site is able to accommodate a range of metal ions, which indicates a flexible metal binding site. To gain insight into this issue $^{15}\text{N}\{\text{H}\}$ -NOEs as well as T_1 and T_2 relaxation times (ps and ns timescale) were measured in the presence or absence of Zn^{2+} .

Both the $^{15}\text{N}\{\text{H}\}$ -NOEs and relaxation data are relatively featureless and show the characteristics of a rigid protein. The one clear exception is the N-terminus of the protein that shows increased flexibility in the absence of metal ions (Fig. S5). However, in the presence of the metal ion, this extra flexibility at the N-terminus is lost.

Substrate binding. Amino acid residues involved in binding to chitin were mapped using an NMR approach that exploits the pH dependency of substrate binding (Fig. S6; nanofibrillar β -chitin) in a $^2\text{H}/^1\text{H}$ exchange experiment. Fig. 6A shows that chitin-binding protected two regions from exchange, Gln53-Ser58 and Leu110-Thr116, providing direct experimental evidence that these surface-exposed regions are involved in substrate binding (Fig. 6B-D).

The correlation between pH-dependent desorption of CBP21 from chitin (pH 3-4) (Fig. S6) and the observed loss of the metal co-factor (at a pH of approximately 3, depending on the metal and its redox state; see above), prompted us to attempt desorbing CBP21 from chitin with a metal chelator only (EDTA). This was successful at 200 mM EDTA, providing a useful alternative purification protocol (Fig. S7).

Discussion

Considering the dominance of LPMOs in the secretomes of biomass-degrading microorganisms (e.g. (18)), the abundance of LPMO-encoding genes in such organisms, and the documented beneficial effects of LPMOs on biomass conversion, it seems that we have only seen the beginning of what may be a very important development in enzymatic biomass-refining. Many important aspects of these recently discovered enzymes remain unresolved, including the catalytic mechanism and the structural determinants of substrate specificity. The NMR and ITC studies described above provide unprecedented insight into several key properties of these enzymes.

The data presented in this study unambiguously show that CBP21 is a copper-dependent LPMO. Cu^{2+} binds CBP21 with nanomolar affinity (Table 1 and Figs 2 and 3) and is essential for catalysis (Fig. 4). Binding of cyanide, a di-oxygen mimic and potent inhibitor of CBP21, to the metal (Fig. S4) indicates that the metal ion is actively involved in oxidative cleavage of the substrate by CBP21. Importantly, the redox potential of the $\text{Cu}^{2+}/\text{Cu}^{1+}$ couple in CBP21 is elevated relative to that of aqueous $\text{Cu}^{2+}/\text{Cu}^{1+}$ (115 mV) which reflects tighter binding of Cu^{1+} relative to Cu^{2+} . Tighter binding of Cu^{1+} is confirmed by the competition experiments in anaerobic conditions, which showed that CBP21- Cu^{1+} was not oxidized by a 10-fold surplus of Cu^{2+} in the solution (Fig. 2E). The 115 mV increase in redox potential is in accordance with previous studies showing that complexation of Cu^{2+} in a type 2 copper binding site increases the redox potential by 40 to 240 mV relative to the potential of aqueous Cu^{2+} (19-21). The fact that CBP21 seems to preferably bind Cu^{1+} coincides with the notion that molecular oxygen tends to bind copper proteins in their reduced monovalent state (22). These data and considerations are compatible with the initial steps of a catalytic mechanism proposed for a GH61-type LPMO by Phillips *et al.* (4): Cu^{2+} is reduced on the enzyme to Cu^{1+} by an electron supplied by a chemical compound or an enzyme such as cellobiose dehydrogenase; upon oxygen binding to the metal ion, the electron is transferred to generate a superoxo intermediate (Fig. 1F).

Notably, the mapping of enzyme-substrate interactions unequivocally shows that the metal-binding site is in direct proximity to the substrate when CBP21 is bound to the chitin surface (Fig. 6).

While CBM33-type and GH61-type LPMOs seem to catalyze essentially the same reaction (4, 5, 12, 13, 23), and have similar active sites (Fig. 1D,E), their metal binding sites do show some notable differences. Quinlan *et al.* (12) indicated that the K_d for Cu^{2+} binding to *TaGH61A* is below 1 nM, suggesting that the binding affinity is at least 50-fold higher than for CBP21. In CBP21, Cu^{2+} is coordinated by two histidines, whereas *TaGH61A* and other GH61s in addition have a tyrosine that contributes to ion coordination through the hydroxyl group and a glutamine that indirectly contributes to metal coordination through positioning a water molecule that interacts with the copper ion (Fig. 1E). Moreover, the N-terminal histidine is methylated in all structures so far published for GH61 enzymes (12). This modification may increase the affinity for the metal ion since 3-methyl histidine has a pK_a elevated by ~ 0.5 compared to a normal histidine (24). Alternatively, the methylation may have favorable structural/dynamic effects, such as pre-positioning the N-terminal histidine to optimally accommodate the

copper ion. Notably, differences between the binding sites are also illustrated by the fact that no other metals than copper ions were found to bind to *TaGH61A* (12), whereas CBP21 binds Zn^{2+} with micromolar affinity.

Interestingly, Cu^{1+} dissociates from His28 and His114 at pH values that are also known to induce dissociation of substrate-bound CBP21 (see Fig. S6 for β -chitin and (25) for regenerated chitin). While this suggests that substrate binding depends on the presence of a bound metal ion, it should be noted that the EDTA concentrations needed to elute CBP21 from a chitin column were much higher than those needed for completely inactivating the enzyme. Thus, metal depletion alone is insufficient for elution and other interactions do contribute to binding (as also suggested by early mutagenesis work described in (8)).

Obtaining information on LPMO-substrate interactions is challenging due to the bi-phasic nature of the experimental system (solid substrate, soluble enzyme). Using an approach that exploits the pH dependency of both the chitin-CBP21 interaction and the $^2H/^1H$ exchange rate, we were able to directly identify residues involved in binding CBP21 to the chitin surface (Fig. 6). Identified residues matched with residues previously suggested to be involved in substrate binding based on combined structure and sequence analysis and mutagenesis (8), and included the only solvent exposed aromatic amino acid in the previously proposed binding area, Tyr54 (Fig. 6 and (8)). Interestingly, the identified binding residues line up in a narrow stretch along the substrate binding surface that could match the width of a single polysaccharide chain (Fig. 6B). It is important to note though that the $^2H/^1H$ exchange experiments reflect protection of amide protons and that it is conceivable that certain residues interact with chitin without their amide protons being protected from rapid exchange (the presence of additional interacting residues is suggested by mutagenesis and sequence conservation data; Fig. 6C,D). CBP21 does not bind single chitin chains, but rather an ordered array of chains (like the crystalline surface of a chitin fibril; (26)). Therefore, if there really would be only a narrow stretch of interacting residues, one might speculate that the protein binds with this stretch being oriented perpendicularly to the polysaccharide chains. Interestingly, a similar (speculative) suggestion has very recently been made on the bases of the crystal structure of a GH61 protein (27).

Despite the availability of seven LPMO crystal structures (four CBM33s and five GH61s), most aspects of these enzymes' intriguing catalytic activity have remained unknown. The first NMR structure of a LPMO described here has allowed the study of several functional aspects. Finally, as molecular motion and NMR share the same time scale, we also obtained dynamic information about the protein. The results show generally very little flexibility, with the exception of the metal binding site which in the absence of a metal ion shows some highly local flexibility. We conclude that the unique ability of LPMOs to oxidatively cleave polysaccharide chains without expelling these chains from their crystalline context depends on a fixed geometry around the oxygen-coordinating metal binding site. The rigid nature of CBP21 seems well adapted to bind the highly ordered crystalline chitin surface.

Materials and Methods

For details see *SI text*

NMR spectroscopy

Isotope labeled recombinant CBP21 used in NMR experiments was produced in *E. coli* cultivated in isotope enriched (^{15}N or ^{13}C , ^{15}N) M9 minimal medium and purified as described in (8). NMR assignment of CBP21 was done previously (28) and NMR data for CBP21 were obtained using a Bruker Avance 600 MHz spectrometer.

Detection of residues involved in binding of CBP21 to chitin was accomplished with a method that exploits the pH dependency of binding. The method involved binding CBP21 to β -chitin in buffered H_2O followed by buffer exchange to D_2O at pH 6.0. At this stage, backbone amide groups shielded from solvent by binding to chitin will retain their protons whereas amide protons on solvent exposed parts of the enzyme are exchanged with deuterium. CBP21 was then released from the substrate by pelleting the CBP21-bound chitin by centrifugation and re-suspension in H_2O buffered to pH 3.5. At this pH proton exchange is slow ($k_{\text{exchange}} \sim 0.25 \cdot 10^{-3} \text{ s}^{-1}$) and the concomitantly recorded ^{15}N -HSQC spectrum clearly revealed back bone amide groups having protons bound (giving very intense signals) versus deuterium bound (weak signals). By comparing the two spectra, residues involved in binding could be identified by evaluating the backbone amide group intensity differences. For details, see *SI text*.

Enzyme activity and binding assays

CBP21 was produced in the apo-form by chitin affinity chromatography (8) using 0.2 M EDTA to elute the protein. Metal dependency of CBP21 activity was assayed by incubating CBP21_{apo} in the presence of 2.5 mg/ml β -chitin fibers (produced according to the method described by Fan *et al.* (29)), 1.0 mM ascorbic acid (electron donor), 50 μM EDTA and 25 μM metal ion salt in 20 mM Tris-HCl pH 8.0 at 37°C. Soluble products were analyzed at 1, 5 and 24 h incubation using HILIC based chromatographic methods and MALDI-TOF MS analysis as described previously (5).

For details, see *SI text*.

ITC

Dissociation constants and thermodynamic data for binding of Zn^{2+} and Cu^{2+} to CBP21 was achieved by measuring the heat produced when injecting 4 μl aliquots (40 in total) of 150 μM metal ion solutions into the reaction cell of a VP-ITC system from MicroCal, Inc (Northampton, MA) containing 1.42 ml of a 5 μM CBP21_{apo} solution buffered to pH 6.5 with PIPES at 6°C. For details, see *SI text*.

Redox potential determination

Determination of the cell potential (E°) for the CBP21- Cu^{2+} /CBP21- Cu^{1+} redox couple was done by allowing reduced TMP (50 μl and 300 μM) to react with CBP21- Cu^{2+} (50 μl and 70 μM) and reach equilibrium under anaerobic conditions and the extent of reaction, and hence the equilibrium constant, was determined by measuring absorbance from the formed TMP radical cation at 610 nm. The equilibrium constant was used to calculate E° for the CBP21- Cu^{2+} /CBP21- Cu^{1+} redox couple since this is proportional to the difference

in the cell potentials between the two redox couples in the electron transfer reaction. For details, see *SI text*.

Acknowledgments

This work was funded by grants 186946, 196885 & 214613 (GVK, VGH), 209335/F20 (MS) and 182695/I40 (GSB and FLA) from the Norwegian Research Council (NFR). We thank Anne Cathrine Bunæs for assisting with protein purification and Reinhard Wimmer for assisting with TALOS+ and energy refinement.

References

1. Henrissat B, Driguez H, Viet C, & Schulein M (1985) Synergism of cellulases from *Trichoderma-reesei* in the degradation of cellulose. *Biotechnology (N Y)* 3:722-726.
2. Merino ST & Cherry J (2007) Progress and challenges in enzyme development for biomass utilization. *Biofuels* 108:95-120.
3. Medie FM, Davies GJ, Drancourt M, & Henrissat B (2012) Genome analyses highlight the different biological roles of cellulases. *Nat Rev Microbiol* 10:227-234.
4. Phillips CM, Beeson WT, Cate JH, & Marletta MA (2011) Cellobiose dehydrogenase and a copper-dependent polysaccharide monooxygenase potentiate cellulose degradation by *Neurospora crassa*. *ACS Chem Biol* 6:1399-1406.
5. Vaaje-Kolstad G, *et al.* (2010) An oxidative enzyme boosting the enzymatic conversion of recalcitrant polysaccharides. *Science* 330:219-222.
6. Cantarel BL, *et al.* (2009) The Carbohydrate-Active EnZymes database (CAZy): an expert resource for Glycogenomics. *Nucleic Acids Res* 37:233-238.
7. Karkehabadi S, *et al.* (2008) The first structure of a glycoside hydrolase family 61 member, Cel61B from *Hypocrea jecorina*, at 1.6 angstrom resolution. *J Mol Biol* 383:144-154.
8. Vaaje-Kolstad G, Houston DR, Riemen AHK, Eijsink VGH, & van Aalten DMF (2005) Crystal structure and binding properties of the *Serratia marcescens* chitin-binding protein CBP21. *J Biol Chem* 280:11313-11319.
9. Vaaje-Kolstad G, Horn SJ, van Aalten DMF, Synstad B, & Eijsink VGH (2005) The non-catalytic chitin-binding protein CBP21 from *Serratia marcescens* is essential for chitin degradation. *J Biol Chem* 280:28492-28497.
10. Harris PV, *et al.* (2010) Stimulation of lignocellulosic biomass hydrolysis by proteins of glycoside hydrolase family 61: structure and function of a large, enigmatic family. *Biochemistry* 49:3305-3316.
11. Vaaje-Kolstad G, *et al.* (2012) Characterization of the chitinolytic machinery of *Enterococcus faecalis* V583 and high-resolution structure of its oxidative CBM33 enzyme. *J Mol Biol* 416:239-254.
12. Quinlan RJ, *et al.* (2011) Insights into the oxidative degradation of cellulose by a copper metalloenzyme that exploits biomass components. *Proc Natl Acad Sci U S A* 108:15079-15084.
13. Westereng B, *et al.* (2011) The putative endoglucanase PcGH61D from *Phanerochaete chrysosporium* is a metal-dependent oxidative enzyme that cleaves cellulose. *PLoS One* 6:e27807.
14. Shen Y, Delaglio F, Cornilescu G, & Bax A (2009) TALOS+: a hybrid method for predicting protein backbone torsion angles from NMR chemical shifts. *J Biomol NMR* 44:213-223.
15. Arnesano F, Banci L, Bertini I, & Thompsett AR (2002) Solution structure of CopC: A cupredoxin-like protein involved in copper homeostasis. *Structure* 10:1337-1347.

16. Sorlie M, Seefeldt LC, & Parker VD (2000) Use of stopped-flow spectrophotometry to establish midpoint potentials for redox proteins. *Anal Biochem* 287:118-125.
17. Creighton TE (1997) *Proteins: Structure and Molecular Properties* (W.H. Freeman and Company, New York) Second Ed pp 407-410.
18. Znameroski EA, *et al.* (2012) Induction of lignocellulose-degrading enzymes in *Neurospora crassa* by cellodextrins. *Proc Natl Acad Sci U S A* 109:6012-6017.
19. Jacobson F, *et al.* (2007) pH dependence of copper geometry, reduction potential, and nitrite affinity in nitrite reductase. *J Biol Chem* 282:6347-6355.
20. Ljones T, *et al.* (1978) Dopamine β -monooxygenase: electron paramagnetic resonance and oxidation-reduction properties of the enzyme-bound copper. *FEBS Lett* 92:81-84.
21. Rae TD, Schmidt PJ, Pufahl RA, Culotta VC, & V. O'Halloran T (1999) Undetectable Intracellular Free Copper: The Requirement of a Copper Chaperone for Superoxide Dismutase. *Science* 284:805-808.
22. Que L, Jr. & Tolman WB (2008) Biologically inspired oxidation catalysis. *Nature* 455:333-340.
23. Forsberg Z, *et al.* (2011) Cleavage of cellulose by a CBM33 protein. *Protein Sci* 20:1479-1483.
24. Paiva ACM, Juliano L, & Boschcov P (1976) Ionization of methyl-derivatives of imidazole, histidine, thyrotropin releasing factor, and related compounds. *J Am Chem Soc* 98:7645-7648.
25. Suzuki K, Suzuki M, Taiyoji M, Nikaidou N, & Watanabe T (1998) Chitin binding protein (CBP21) in the culture supernatant of *Serratia marcescens* 2170. *Biosci Biotechnol Biochem* 62:128-135.
26. Nishiyama Y, Noishiki Y, & Wada M (2011) X-ray Structure of Anhydrous beta-Chitin at 1 angstrom Resolution. *Macromolecules* 44:950-957.
27. Li X, Beeson WT, Phillips CM, Marletta MA, & Cate JHD (2012) Structural Basis for Substrate Targeting and Catalysis by Fungal Polysaccharide Monooxygenases. *Structure* 20:1051-1061.
28. Aachmann FL, Eijsink VGH, & Vaaje-Kolstad G (2011) H-1, C-13, N-15 resonance assignment of the chitin-binding protein CBP21 from *Serratia marcescens*. *Biomol NMR Assign* 5:117-119.
29. Fan Y, Saito T, & Isogai A (2008) Preparation of chitin nanofibers from squid pen beta-chitin by simple mechanical treatment under acid conditions. *Biomacromolecules* 9:1919-1923.
30. DeLano WL & Lam JW (2005) PyMOL: A communications tool for computational models. *Abstr Pap Am Chem S* 230:1371-1372.
31. Ashkenazy H, Erez E, Martz E, Pupko T, & Ben-Tal N (2010) ConSurf 2010: calculating evolutionary conservation in sequence and structure of proteins and nucleic acids. *Nucleic Acids Res* 38:529-533.

Figure Legends

Figure 1. Structure of CBP21 and metal ion binding. (A) Stereo image showing a superposition of the X-ray crystallographic structure of CBP21 (PDB ID 2BEM; blue) and the 20 energy-minimized conformations of CBP21 solved by solution NMR (PDB ID 2LHS) colored red (helix), yellow (strand) and green (coil). The N- and C-terminal residues are indicated (note that the N-terminus is part of the catalytic center). The mean RMSD between X-ray crystallographic structure and the 20 NMR structures was calculated to be 1.54 +/- 0.07 Å using the Swiss-Pdb Viewer software. (B,C) Change in amino acid chemical shifts (^{15}N - and ^{13}C -HSQC) upon adding 2.0 mM Zn^{2+} (B) or Cu^{2+} (C) to 0.5 mM CBP21_{apo}, where the degree of change is indicated by the colouring scheme. The CBP21 structure is shown by a “top” view (left) and “side” view (right). The signals of residues in close proximity to the Cu^{2+} ion “vanish” due to the paramagnetic relaxation enhancement (PRE) effect induced by Cu^{2+} . The data for copper (panel C) also indicated a secondary metal binding site comprising (non-conserved) residues Glu85 and His74 that showed weak and ambiguous interactions. These interactions were only observable at the highest tested Cu^{2+} concentration (2 mM) and were thus regarded as artifacts. (D,E) Metal binding sites observed in the crystal structures of CBP21 (D; with an unknown metal ion bound (8)) and TaGH61A (E; with copper bound (12)). Metal ions and water molecules are shown as bronze and red colored spheres, respectively. Residue numbering is based on the explicit sequence (i.e. the signal sequence is taken into account; 27 residues for CBP21 and 21 residues for TaGH61A; H28 and H22 are the N-terminal residues, respectively). Note that TaGH61A H22 is post translationally methylated at Nε2 (panel E; (12)). Structure illustrations were prepared using PyMOL (30). (F) Schematic overview of the reaction catalyzed by LPMOs based on existing experimental evidence. The LPMO, coordinating a reduced copper ion (Cu(I)) activates molecular oxygen that through an unknown reaction mechanism results in cleavage of the glycosidic bond, oxidation of the C1 carbon by a single oxygen (red oxygen) and hydrolysis (blue oxygen) to yield the aldonic acid end product. See (4) for further suggestions concerning the mechanism. Note that copper binding involves three nitrogen atoms, as indicated, namely the N-terminal amino group and an imidazole nitrogen in each of the two conserved histidines.

Figure 2. Spectral changes in CBP21 upon interaction with zinc and copper ions. (A) Overlay of ^{13}C HQSC spectra for 0.5 mM CPB21 in the presence of 0 (black), 0.25 (red), 0.50 (blue) and 2.0 (green) mM Zn^{2+} . New signals appear for His28 and His114 upon binding of Zn^{2+} and increase in intensity upon titration, displaying a slow exchange situation. This indicates that both histidines have high affinity for Zn^{2+} . The signal for Trp108, a residue not affected by metal binding, is the same in all spectra. (B) Overlay of ^{13}C HQSC spectra for 0.5 mM CBP21 and 1 mM Zn^{2+} in the presence (red) or absence (black) 0.5 mM Cu^{2+} . Upon binding of Cu^{2+} ions the signals for the metal binding site (His28 and His114) broaden beyond detection due to paramagnetic relaxation enhancement (PRE). The absence of red signals thus shows that Cu^{2+} binds stronger than Zn^{2+} . (C) Overlay of ^{13}C HQSC spectra for 0.5 mM CBP21 and 1 mM Zn^{2+} in the presence (red) or absence (black) of ~0.65 mM Cu^{1+} under reducing conditions. As Cu^{1+} is not paramagnetic, signals for His28 and His114 are still present in the spectrum. (D)

Overlaid ^{13}C HQSC spectra for 0.5 mM metal-free CBP21 in the presence (red) or absence (black) of 0.5 mM Cu^{2+} . Binding of copper eliminates His28 and His114 signals due to PRE. (E) ^{13}C HQSC spectrum for 0.5 mM CBP21 in the presence of 0.5 mM Cu^{1+} and 5.0 mM Cu^{2+} , in anaerobic conditions. This spectrum shows that Cu^{1+} bound to CBP21 is not oxidized or replaced by free Cu^{2+} since line broadening effects (PRE) of the His28 and His114 signals are not observed. The presence (F) or absence (G) of Cu^{2+} in solution is verified by the proton spectrum where a high concentration of Cu^{2+} ions results in generally enhanced relaxation conditions in the sample, e.g. leading to disappearance of the acetate signal at ~ 1.9 ppm.

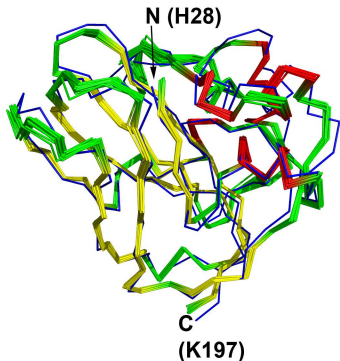
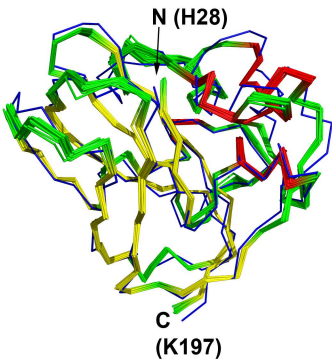
Figure 3: Thermograms (upper panels) and binding isotherms with theoretical fits (lower panels) obtained for the binding of 150 μM Cu^{2+} (A) or Zn^{2+} (B) to 5 μM CBP21_{apo} at 6°C.

Figure 4. Cu^{2+} -reactivation of CBP21. Chromatographic analysis of soluble products obtained upon incubating 2.0 μM metal-free CBP21 with 2.5 mg/ml β -chitin fibers in the presence of 1.0 mM ascorbic acid, 50 μM EDTA and 25 μM CuSO_4 (light blue), ZnSO_4 (dark blue), MgSO_4 (red), MnSO_4 (green) or buffer (control; purple), at 37°C in 20 mM Tris-HCl pH 8.0 for 24 h. The insert in the upper left corner shows formation of (GlcNAc)₅GlcNAc-aldoic acid (DP_{6ox}) over time by CBP21- Cu^{2+} . See Fig. S3 for further details on product analysis.

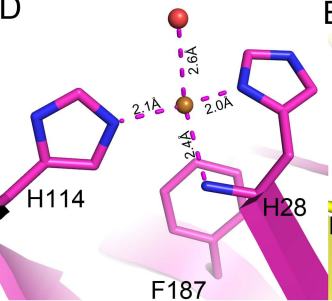
Figure 5: Titration of His28 and His114 (^{13}C HSQC spectra). Chemical shifts of $\text{C}^{\epsilon 1}$ (circles) and $\text{H}^{\epsilon 1}$ (crosses) are plotted as a function of pH (4.0-8.5) for His28 (A) and His114 (B) for CBP21_{apo}. The data was fitted to the Henderson-Hasselbach equation (fitted curve indicated by lines) yielding pK_a values 7.03 ± 0.25 and 5.85 ± 0.09 for His28 and His114, respectively. (C,D) Ratio of protonated histidine vs. metal bound histidine during a similar titration for CBP21 saturated with Zn^{2+} and Cu^{1+} , respectively. In the presence of Cu^{1+} , pK_a values are 3.3-3.5 for His28 (crosses) and 3.5-3.7 for His114 (circles). In the presence of Zn^{2+} both residues have a pK_a of 4.3-4.4.

Figure 6: Chitin binding by CBP21. (A) Signal intensities in ^{15}N -HSQC spectra of CBP21 in the presence of chitin divided by their intensities in the absence of chitin after deuterium (^2H) exchange in buffer (10 mM phosphate buffer, pH 6.0, 10 mM NaCl) for 30 min. Exchange was quenched by reducing the pH to 3.5 (using 50 mM acetate buffer). While most signal intensity ratios are close to 1, some amino acids (labeled) show higher values owing to significant protection of the HN against exchange in the presence of chitin, presumably by chitin binding. (B) Residues identified as involved in chitin binding from the data in panel A mapped on the surface of CBP21 by yellow surface coloring. (C). Residues involved in chitin binding by CBP21, as determined by site-directed mutagenesis in a previous study (8) shown by yellow surface coloring. (D) Highly conserved residues on the CBP21 substrate binding surface determined by sequence analysis available in the ConSurf database (31) shown by yellow surface coloring. The database entry used was PDB ID 2BEM. Residues scoring >8 were considered highly conserved (9 being maximum, 1 minimum).

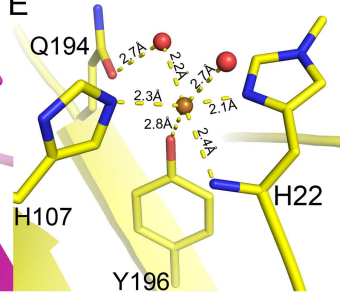
A



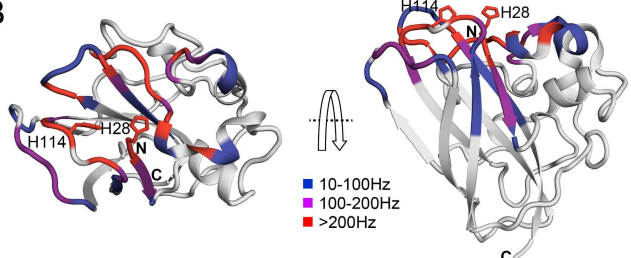
D



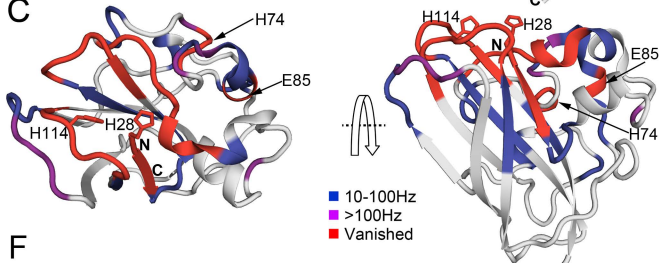
E



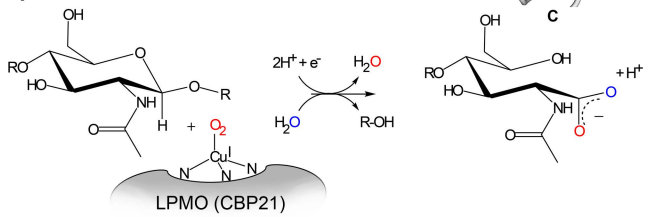
B

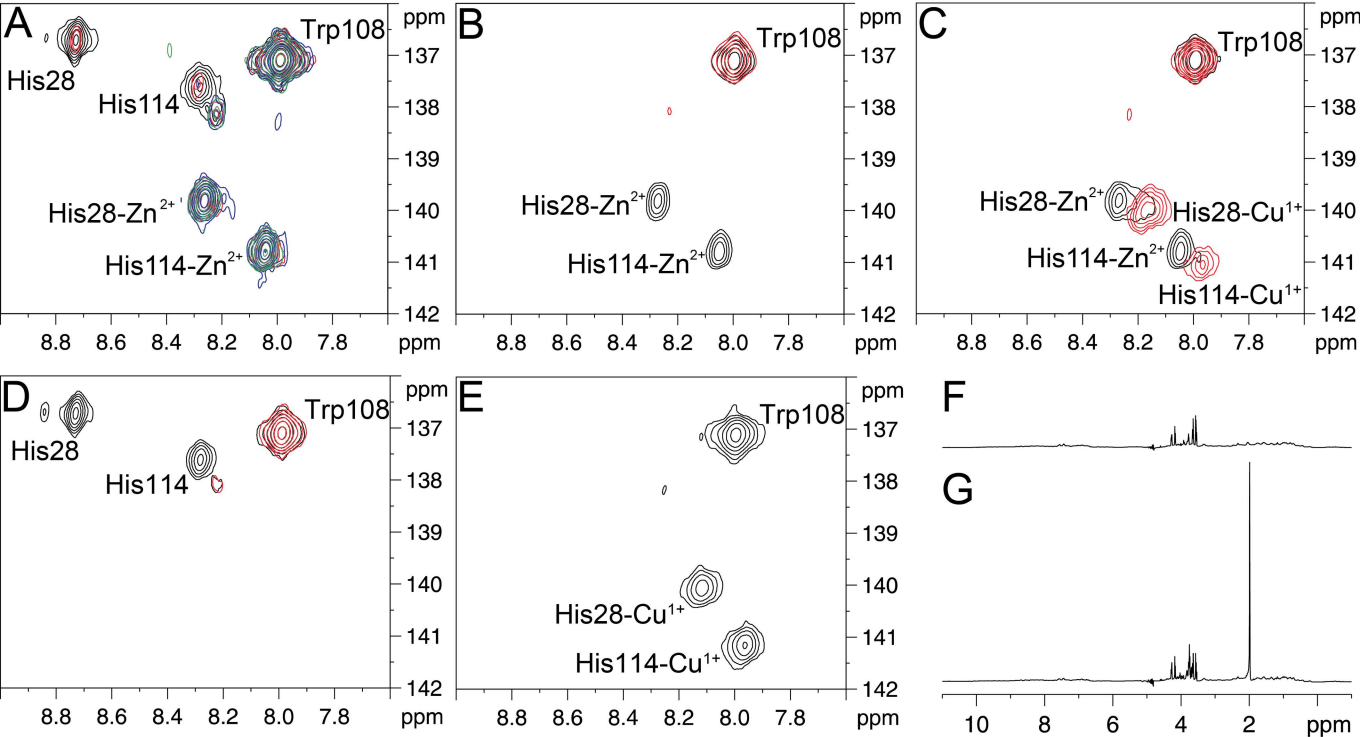


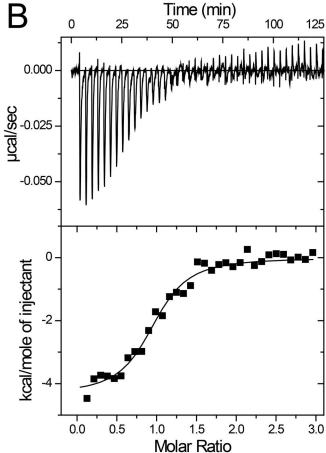
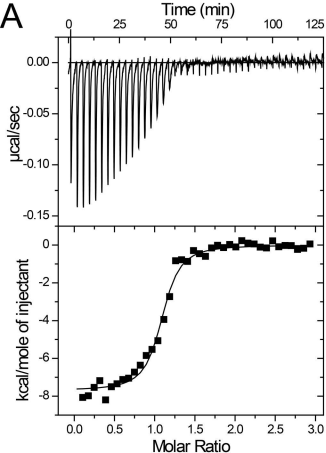
C

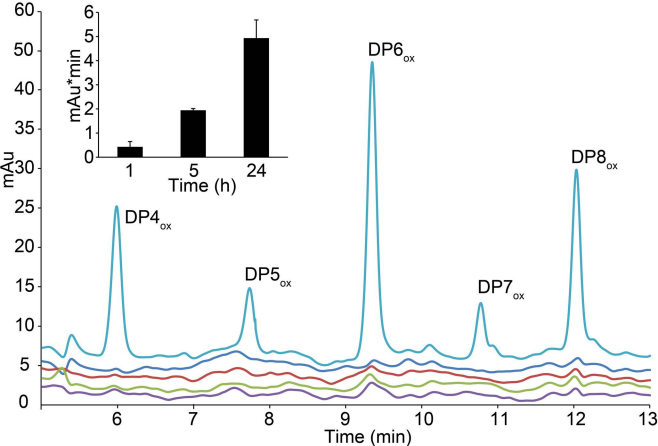


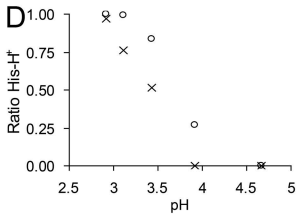
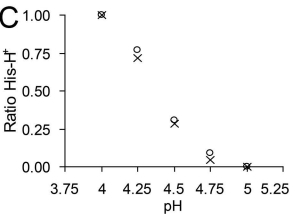
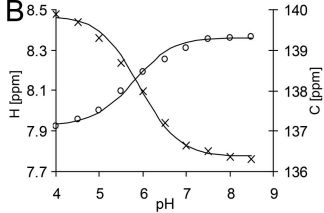
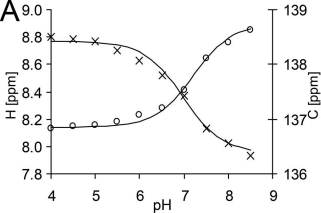
F

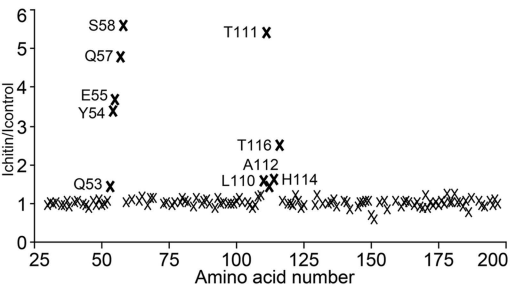
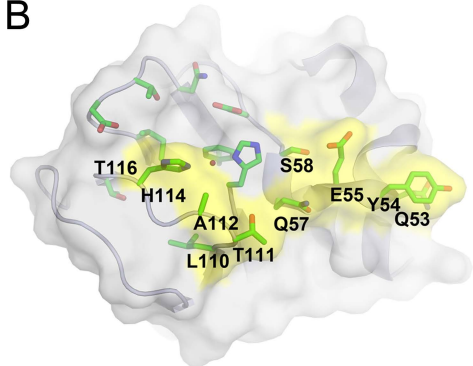
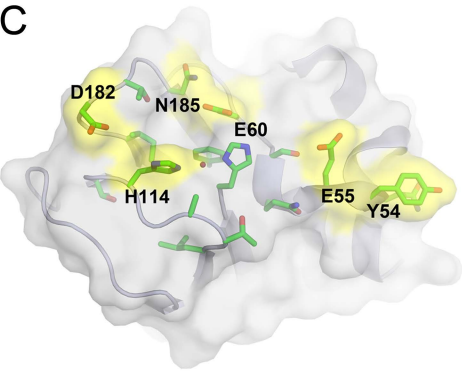
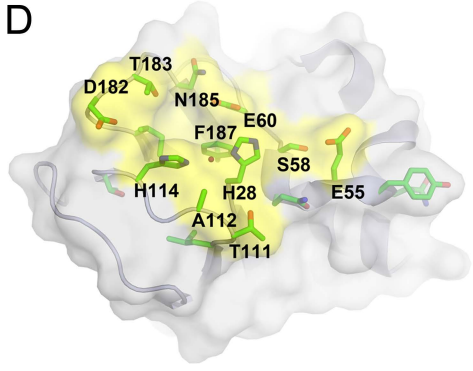










A**B****C****D**

SI Materials and Methods

Sample preparation. Cloning, protein expression- and purification of uniformly isotope labeled (^{15}N and/or ^{13}C) and non-labeled recombinant CBP21 (170 amino acids) and conditions for NMR measurements have been described previously (1, 2). For some experiments (specified in the text) CBP21 was eluted from the chitin bead column (NEB) by 0.2 M EDTA pH 8.0 instead of 20 mM acetic acid that is used in the original purification protocol. All NMR experiments were conducted with CBP21 that had been EDTA treated to remove metals bound (CBP21_{apo}; see (2) for details). After purification, the elution buffer were changed to an appropriate buffer (experiment dependent) using protein spin concentrators (Amicon, 10 kDa cut off). A 50 mM Tris-HCl pH 8.0 buffer containing 0.05 mM EDTA was used for the Cu-reactivation experiment (see further down). Samples for the NMR structure determination studies contained 0.8-1.2 mM CBP21 in 20 mM phosphate buffer pH 5.5, 10 mM NaCl in 90% H₂O / 10% D₂O or 99.9% D₂O. Protein concentration was determined by measuring A₂₈₀ of the protein sample using a Nanodrop ND-1000 spectrophotometer (NanoDrop products, Wilmington, DE) and deducing the protein concentration based on the theoretical extinction coefficient (calculated using the ProtParam tool: <http://web.expasy.org/tools/protparam/>).

NMR spectroscopy. NMR spectra of ~ 0.5 mM CBP21 samples were recorded at 298 K on a Bruker Avance 600 MHz spectrometer equipped with a 5 mm z-gradient CP-TCI(H/C/N). Two-dimensional ^1H , ^1H -NOESY and three-dimensional ^{13}C - and ^{15}N -edited ^1H , ^1H -NOESY spectra were recorded in D₂O and H₂O, respectively. NMR data were processed using BRUKER XWinNMR version 3.5 and TopSpin version 2.1/3.0. NMR spectral analysis was performed using CARA version 1.4.1/1.5.3 (3). ^{15}N - $\{^1\text{H}\}$ heteronuclear NOEs were derived with Protein Dynamic Center software version 1.2 from Bruker BioSpin using two independently measured and integrated ^{15}N - $\{^1\text{H}\}$ heteronuclear correlated spectra that had been recorded using an enhanced sensitivity sequence employing pulsed field gradient (4) with and without ^1H saturation. Nuclear magnetic relaxation (T_1 and T_2) measurements of ^{15}N nuclei were analyzed with Protein Dynamic Center software version 1.2 from Bruker BioSpin using exponential fitting of data from ^{15}N -HSQC spectra that had been acquired with different relaxation delays (4,5).

Structure calculation. NOE cross peaks were identified, assigned and integrated using the program NEASY in the CARA suite (3). The CALIBA (6) subroutine in CYANA 3.0 was used to convert cross peak intensities from NOESY spectra into distance constraints. Dihedral angle constraints (ϕ, ψ) were obtained from secondary chemical shifts with TALOS+ (7). Two disulfide bridges observed in the crystal structure of CBP21, Cys41-Cys49 and Cys135-Cys162, were also used. Based on the input described, the structure was calculated using the torsion angle dynamics program CYANA 3.1 (6). Structure calculations started from 256 conformers with random torsion angle values. 20 conformers with the lowest final CYANA target function values were energy-minimized with YASARA (8) in two steps, first *in vacuo*, then using water as explicit solvent using the particle mesh Ewald method (9), both steps applying the YASARA force field (10). Geometrical constraints and structural statistics are summarized in Table S1. In total, 4330 NOE-based upper limit distances and 231 torsion angle restraints were used to derive the CPB21 structure. The geometrical constraint and coordinate files of the minimized CBP21 conformers have been deposited in the PDB under accession number 2LHS.

Chemical shift Mapping. The chemical shift changes of N and H^N atoms from the backbone of CBP21 upon titration are given as an absolute change in chemical shift by the following formula:

$$\Delta\delta_{abs} = \sqrt{(\Delta\delta_H)^2 + x(\Delta\delta_N)^2}$$

| | |
|----------------------|--|
| $\Delta\delta_{abs}$ | absolute change in chemical shift [Hz] |
| $\Delta\delta_H$ | chemical shift change of the amide proton [Hz] |
| $\Delta\delta_N$ | change in chemical shift of the amide nitrogen atom [Hz] |
| x | constant to achieve equal contribution from changes in N and H ^N - shifts. The constant was set to 5. |

The chemical shift data for His114 (one of the two histidines in the metal binding site) was used to calculate dissociation constants by fitting the experimental data to the following equation:

$$\Delta\delta = \sqrt{(\Delta\delta_H)^2 + 5(\Delta\delta_N)^2}$$

⇓

$$\Delta\delta_{obs} = \delta_{obs} - \delta_{free}$$

$$\Delta\delta_{bound} = \delta_{bound} - \delta_{free}$$

⇓

$$\frac{\Delta\delta_{obs}}{\Delta\delta_{bound}} = \frac{[PL]}{[P]_0}$$

⇓

$$K_a = \frac{[PL]}{[L] \cdot [P]} = \frac{[PL]}{([L]_0 - [PL]) \cdot ([P]_0 - [PL])} = \frac{1}{K_d}$$

⇓

$$\frac{\Delta\delta_{obs}}{\Delta\delta_{bound}} = \frac{[PL]}{[P]_0} = \frac{1}{2[P]_0} \left[([P]_0 + [L]_0 + K_d) \pm \sqrt{([P]_0 + [L]_0 + K_d)^2 - 4[P]_0[L]_0} \right]$$

where

| | |
|----------------------------------|--|
| $\Delta\delta_N, \Delta\delta_H$ | chemical shift change in the nitrogen or proton dimension [Hz] |
| δ_{free} | chemical shift of the atom in the free protein without ligand in solution [Hz] |
| δ_{bound} | chemical shift of the atom in the protein-ligand-complex [Hz] |
| δ_{obs} | chemical shift of the atom in the protein at a certain ligand concentration [Hz] |
| $\Delta\delta_{obs}$ | observed chemical shift changes at a certain point in titration [Hz] |
| $\Delta\delta_{bound}$ | chemical shift changes of the atom in the protein due to ligand binding [Hz] |
| $[PL]$ | protein-ligand complex concentration [mol/L] |
| $[P]$ | free protein concentration [mol/L] |
| $[L]$ | free ligand concentration [mol/L] |
| $[P]_0$ | total protein concentration (free and bound) [mol/L] |
| $[L]_0$ | total ligand concentration (free and bound) [mol/L] |
| K_a | association constant [L/mol] |
| K_d | dissociation constant [mol/L] |

Metal ion titration. Metal ion binding properties were studied by titration of approximately 0.5 mM ^{15}N or ^{13}C , ^{15}N CBP21_{apo} in 20 mM ammonium acetate buffer pH 5.5, 10 mM NaCl with Ca^{2+} , Co^{2+} , Fe^{3+} , Mg^{2+} , Zn^{2+} , Cu^{1+} and Cu^{2+} , all as chloride salts. CBP21 titration was achieved by adding small aliquots of 50 mM or 250 mM metal ion stock solutions in 20 mM sodium acetate buffer pH 5.5 containing 10 mM NaCl. When titrating CBP21 with Mg^{2+} , stock solutions of 50 mM, 250 mM and 1 M MgCl_2 in 20 mM phosphate buffer at pH 5.5 and 7.0 with 10 mM NaCl were used. By using concentrated stock solutions the volume increase in the sample was kept to a minimum. A ^{15}N -HSQC spectrum was recorded for each titration point. The CBP21_{apo} concentrations used ranged from 0.25 to 0.50 mM. To obtain further details for Zn^{2+} and Cu^{2+} titrations with these ions were also monitored by chemical shift mapping in the aromatic region of ^{13}C -HSQC spectra.

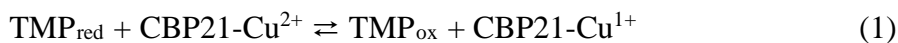
For competitive titrations, a NMR sample was prepared containing 0.5 mM ^{13}C , ^{15}N CBP21_{apo} in 1 mM ZnCl_2 , 20 mM sodium acetate buffer pH 5.5, 10 mM NaCl and titrated by adding an appropriate (small) volume of a 50 mM Cu^{2+} stock solution. For the Cu^{1+} experiment a NMR sample was prepared with 0.5 mM ^{13}C , ^{15}N CBP21 in 1 mM ZnCl_2 , 20 mM ascorbic acid, 20 mM sodium acetate buffer pH 5.5 and 10 mM NaCl. Cu^{1+} has a low solubility (~0.63 mM) and instead of titrating the NMR sample, solid CuCl in pellet form was added directly to the NMR tube in quantities ensuring saturation (~1 mg). The $\text{Cu}^{1+}/\text{Cu}^{2+}$ competition experiment was done by transferring the CBP21- Cu^{1+} sample to a new NMR tube followed by titration with Cu^{2+} .

Cyanide inhibition. A NMR sample with 0.4 mM ^{13}C , ^{15}N CBP21 in 20 mM HEPES pH 7.0 with 2 mM ZnCl_2 and 10 mM NaCl (550 μl , 90% H_2O / 10% D_2O) was added to a NMR tube with 0.4 mg sodium cyanide (yielding a 14 mM cyanide concentration). ^{15}N -HSQC and ^{13}C -HSQC spectra were recorded. The pH in the sample was measured to pH 7.4 after NMR recording. A control experiment (leaving out the zinc) was performed in the same way; here the pH of the sample was measured to pH 7.5 after the NMR recording.

pH-dependence. pH titration of CBP21 was performed on ~0.4 mM ^{13}C , ^{15}N CBP21 in 20 mM phosphate buffer with 10 mM NaCl in 90% H_2O / 10% D_2O in the pH range 4.0-8.5 in steps of 0.5 pH units. Another pH titration with zinc present was performed on 0.5 mM ^{13}C , ^{15}N CBP21 in 20 mM ammonium acetate buffer with 10 mM NaCl in 90% H_2O / 10% D_2O in the pH range 5.0-8.0 in steps of 1.0 pH units and in the pH range 4.0-5.0 in steps of 0.25 pH units. Buffers were exchanged by washing the protein three times using a Vivaspin column (10 kDa molecular cut-off). The pH was checked prior to recording of the NMR spectrum. This procedure ensured minimal change in ionic strength and well defined pH values for each titration step. For the pH titration in presence of Cu^{1+} , 0.5 mM ^{13}C , ^{15}N CBP21 in 20 mM sodium acetate buffer, 20 mM ascorbic acid, 10 mM NaCl with CuCl directly added was prepared (ensuring Cu^{1+} saturation in solution [~0.63 mM]). The sample was titrated by adding small amounts (0.5-2 μl) of 1M HCl and the pH of the sample was measured with a mini pH probe. A ^{15}N -HSQC and a ^{13}C -HSQC spectrum were recorded for each titration point. The data were fitted using Sigmaplot version 11.0.

Determination of the cell potential (E°) for the CBP21- $\text{Cu}^{2+}/\text{CBP21-Cu}^+$ redox couple. Solutions of oxygen free *N,N,N',N'*-tetramethyl-1,4-phenylenediamine (TMP_{red}) in its reduced form (50 μl , 300 μM and 200 μM , respectively) and CBP21- Cu^{2+} (50 μl and 70 μM) in 20 mM PIPES buffer pH 6.0, $t = 25^\circ\text{C}$ were mixed in a cuvette and placed in a Hitachi U-1900 spectrophotometer. The extent of reaction was determined by measuring absorbance

from the formed TMP radical cation (TMP_{ox}) at $\lambda = 610$ nm, and concentrations of TMP_{ox} , which equal concentrations of CBP21-Cu^{1+} , were calculated by using an extinction coefficient of $14.0 \text{ mM}^{-1}\text{cm}^{-1}$ (11). This allowed for calculations of the equilibrium concentrations for the electron transfer reaction (Equation 1), and hence, the equilibrium constant (Equation 2):



$$K = \frac{[\text{TMP}_{\text{ox}}][\text{CBP-Cu}^{1+}]}{[\text{TMP}_{\text{red}}][\text{CBP-Cu}^{2+}]} \quad (2)$$

The relationship between the free energy change (ΔG_r°), the equilibrium constant (K), and the cell potential (E°) is shown in Equation 3:

$$\Delta G_r^\circ = -RT \ln K = -nFE^\circ \quad (3)$$

where R is the gas constant, T is the temperature in Kelvin, n is the number of electrons transferred in the reaction and F is the Faraday constant. A cell potential of 273 mV vs. normal hydrogen electrode (NHE) for the $\text{TMP}_{\text{ox}}/\text{TMP}_{\text{red}}$ redox couple (12) was used to determine the cell potential of $\text{CBP21-Cu}^{2+}/\text{CBP21-Cu}^{1+}$ (see Figure S3). The equilibrium constant for the redox reaction was determined to be 1.2 ± 0.2 yielding an experimental error of ± 6 mV for the cell potential

Chitin binding

Observing the interaction of an enzyme with an insoluble substrate is a major challenge, also when using solution state NMR. Here, we exploited the pH-dependency of binding of CBP21 to chitin. As illustrated by the purification method, CBP21 binds strongly to chitin at pH 8.0 (and lower pH, such as 6.0), whereas it desorbes at \sim pH 3.5 (Fig. S6). In this pH range there is a large change in the proton exchange rate for backbone amides (13) (from 1.66 s^{-1} at pH 6.0 to $0.25 \cdot 10^{-3} \text{ s}^{-1}$ at pH 3.5). This entails that elution of CBP21 can be combined with quenching of the exchange reaction, which has been exploited to detect CBP21 residues involved in substrate binding. The substrate, β -chitin (France Chitin, Marseille, France), was treated by ultrasonication in a mildly acidic solution (20 mM acetic acid, \sim pH 3.2) in order to yield a fine gel-like suspension of β -chitin fibrils, as described by Fan *et al.* (14). CBP21 binding to β -chitin fibers was analyzed using uniformly labeled ^{15}N CBP21 and $\text{D}_2\text{O}/\text{H}_2\text{O}$ exchange. 6 mg β -chitin fibers were washed with 10 mM phosphate buffer pH 6.0 with 10 mM NaCl in H_2O and pelleted by centrifugation at 16.600g. The β -chitin pellet was re-suspended in 1 ml \sim 0.5 mM CBP21 in 10 mM phosphate buffer pH 6.0 with 10 mM NaCl in H_2O and incubated for 5 min at room temperature. The sample was centrifuged for 2 min at 16.600g and the pellet was resuspended in 10 mM phosphate buffer pH 6.0 with 10 mM NaCl in 99.9% D_2O and incubated for 30 min at room temperature. Hereafter the sample was centrifuged for 2 min at 16.600 g and the pellet was resuspended in 600 μl 50 mM acetate buffer pH 3.5 with 10 mM NaCl in 90% $\text{H}_2\text{O}/10\%$ D_2O and centrifuged for 2 min at 16.600 g. The supernatant was transfer to an NMR tube and recording of a ^{15}N -HSQC spectrum was started (total acquisition time was 15 min). Under the conditions used, only residues that were protected from exchange through their interaction with chitin will show NMR signals. In the control experiment β -chitin fibers were incubated in 10 mM phosphate buffer pH 6.0 with 10 mM NaCl in 99.9% D_2O for 30 min prior to incubation with CBP21, after which the reaction was treated in the same way as above.

The pH dependency of binding to β -chitin was verified by measuring adsorption of CBP21 to β -chitin. CBP21 added to a buffered suspension of 10 mg/ml β -chitin to a final concentration of 0.1 mg/ml and incubated at room temperature for 3h with constant agitation. After removal of the chitin by centrifugation (5 min at 16.000 g), the protein concentration in the supernatant (unbound protein) was estimated by measuring absorption at 280 nm, using the corresponding buffer as blank and a 0.1 mg/ml solution of CBP21 in the respective buffer as a control for 100% unbound. Buffers used to achieve the various pHs were 50 mM citrate-phosphate (pH 3, 4, 5 and 6), 50 mM Tris-HCl (pH 7, 8 and 9) and 40 mM ethanolamine (pH 10).

Cu-reactivation assay. In order to assess the metal dependency of CBP21 activity, 2.0 μ M CBP21 purified by EDTA elution was incubated with 2.5 mg/ml β -chitin nanofibers (generated as described above), 1.0 mM ascorbic acid, 25 μ M metal ion salt (CuSO_4 , ZnSO_4 , MgSO_4 , MnCl_2 , or none as control) and 50 μ M EDTA in 20 mM Tris-HCl pH 8.0. Before use, the β -chitin fiber suspension had been incubated for 16 h in a buffer containing 100 mM EDTA pH 8.0, then pelleted by centrifugation (15.000 g for 5 minutes), washed 5 times in TraceSelect water (Sigma) before finally being resuspended in 20 mM Tris-HCl pH 8.0 (made using TraceSelect water and high purity Tris) to 5.0 mg/ml. A slightly elevated pH compared to the other experiments described in this study was used because of the superiority of these conditions for both MALDI-TOF and HPLC analysis of soluble products. The activity of CBP21 at pH 8.0 is essentially identical to activity at pH 6.0 (15). Reactions were incubated at 37°C with shaking at 1000 rpm in a thermomixer (Eppendorf). Aliquots were taken at 1, 5 and 24 h time points and the reaction was stopped by mixing the sample with acetonitrile to yield a final acetonitrile concentration of 72% (v/v). Analysis of products was performed using MALDI-TOF analysis and hydrophobic interaction liquid chromatography (HILIC) using the methods described in (15). All reactions were performed in triplicate.

Isothermal titration calorimetry. ITC experiments were performed with a VP-ITC system from Microcal, Inc (Northampton, MA) (16). Solutions were thoroughly degassed prior to experiments to avoid air bubbles in the calorimeter. Typically, 5 μ M of CBP21 in 20 mM PIPES buffer (pH 6.5) was placed in the reaction cell with a volume of 1.42 ml, and 150 μ M solutions of the ligands in identical buffers as for the protein solutions were placed in the ITC syringe. Aliquots of 4 μ l were injected into the reaction cell at 180 s intervals with a stirring speed of 260 rpm. The titrations were normally complete after 40 injections.

Analysis of calorimetric Data. ITC data were collected automatically using the Microcal Origin v.7.0 software accompanying the VP-ITC system (16). Prior to further analysis, all data were corrected for heat of dilution by subtracting the heat produced by continuing injections of ligand into the reaction cell after completion of the binding reaction. These heats had the same magnitudes as the heats of titrating ligand into buffer alone. The data were fitted using a non-linear least-squares algorithm using a single-site binding model employed by the Origin software that accompanies the VP-ITC system. All data from the binding reactions fitted well to a single-site binding model, yielding the stoichiometry (n), the equilibrium binding association constant (K_a), and the enthalpy change (ΔH_r°) of the reaction. The value of n was found to be between 0.9 and 1.1 per enzyme molecule for all reactions. The changes in reaction free energy (ΔG_r°) and entropy (ΔS_r°), as well as the dissociation constant (K_d) were calculated using the following relationship: $\Delta G_r^\circ = -RT \ln K_a = RT \ln K_d = \Delta H_r^\circ - T \Delta S_r^\circ$. Errors in ΔH_r° , K_d , and ΔG_r° were obtained as standard deviations of at least three experiments. Errors in ΔS_r° and $-T \Delta S_r^\circ$ were obtained as propagation of errors.

SI Figure Legends

Figure S1. Interaction of CBP21 with metal ions. The backbone of CBP21 (shown in cartoon representation) is coloured by the change in chemical shift (^{15}N HSQC) upon adding 160 mM Ca^{2+} (A) or 160 mM Mg^{2+} (B), or 16 mM Fe^{2+} (C) or 4 mM Co^{2+} (D), using the indicated colouring scheme, grey coloring representing no change. The CBP21 structure is in all panels shown by a “top” view (left) and “side” view (right). The metal binding site (His28 and His114) is shown in stick representation. Similar data for Zn^{2+} and Cu^{2+} are shown in the main text (Fig. 1B,C). Titrations gave the following estimates of the K_d for the primary metal binding site: Ca^{2+} , > 10 mM; Mg^{2+} , 10-20 mM; Fe^{3+} , 1-3 mM; Co^{2+} , < 0.5 mM. Note that the N-terminal amino group (His28) is very likely to be involved in binding of all metals probed, but due to fast exchange, this residue is normally not observed in NMR (colored gray in all panels).

Figure S2. Calculation of CBP21- Cu^{1+} dissociation constant. The K_d of CBP21 binding to Cu^{1+} can be calculated by combining three thermodynamic relations. Firstly, the cell potential (E°) of $\text{CBP21-Cu}^{2+}/\text{CBP21-Cu}^{1+}$ was derived by experimentally determining the equilibrium constant for the electron transfer reaction between the mediator $\text{TMP}_{\text{red/ox}}$ and $\text{CBP21-Cu}^{2+/1+}$ (SI Materials and Methods and thermodynamic relation I). The cell potential was obtained from the equilibrium constant using the relation $RT\ln K = nFE^\circ$. Secondly, the E° derived from (I) is combined with the known E° for reduction of Cu^{2+} in aqueous conditions to yield the free energy change (ΔG_r°) for the reduction of aqueous Cu^{2+} by CBP21-Cu^{1+} (thermodynamic relation II) using the relation $\Delta G_r^\circ = -nFE^\circ$. Finally, combining the ΔG_r° measured for dissociation of CBP21-Cu^{2+} (Fig. 3 and Table 1) with ΔG_r° deduced from the electron transfer reaction between aqueous Cu^{2+} and CBP21-Cu^{1+} , the dissociation of CBP21-Cu^{1+} can be calculated (thermodynamic relation III) using the relation $\Delta G_r^\circ = RT \ln K_d$.

Figure S3. MALDI-TOF spectrum of soluble products obtained upon incubating 2.0 μM metal-free CBP21 with 2.5 mg/ml β -chitin fibers in the presence of 1.0 mM ascorbic acid, 50 μM EDTA and 25 μM CuSO_4 for 24 h at 37°C (see Fig. 4 in the main text). The spectrum shows the Na- and K- single and double adduct clusters of DP(4-8)ox (see [15] for extensive discussion of product analysis and mass spectrometric data).

Figure S4. Cyanide binding. Spectra overlay for the area of interest from the aromatic ^{13}C HQSC spectra for CBP21 with Zn^{2+} bound before (black) and after (red) addition of cyanide. The fact that both His28- Zn^{2+} and His114- Zn^{2+} have significant chemical shifts when cyanide is present while minimal changes was observed for metal free CBP21 indicates that cyanide interacts directly with Zn^{2+} . A control experiment where sodium cyanide was added to $\text{CBP21}_{\text{apo}}$ showed no changes to either the ^{13}C HQSC or the ^{15}N HQSC spectra.

Figure S5. ^{15}N relaxation data and ^{15}N - $\{^1\text{H}\}$ heteronuclear NOEs for CBP21. (A) Longitudinal relaxation time/transverse relaxation time (T_1/T_2) for metal-free CBP21. (B) Steady-state ^{15}N - $\{^1\text{H}\}$ -NOEs measured for the backbone amide nitrogen atoms for $\text{CBP21}_{\text{apo}}$. (C) T_1/T_2 for CBP21 with Zn^{2+} bound. (D) Steady-state ^{15}N - $\{^1\text{H}\}$ -NOEs for CBP21 with Zn^{2+} bound. In the presence of Zn^{2+} , the N-terminus becomes more rigid with dynamic properties similar to core residues of CBP21. Secondary structure elements of the protein are indicated above panel A. The $T_1:T_2$ ratio is a direct measure for the correlation time for overall rotational tumbling of the protein. The average $T_1:T_2$ ratio for CBP21 was calculated to be 10.3 ± 0.9 , which, assuming a spherical particle, corresponds to an overall rotational correlation time $\tau_c = 9.8 \pm 0.5\text{ns}$ (5). Note that the main effect of adding the metal ions (panel

C vs panel A and panel D vs panel B) is a flattening of the signals for the protein's N-terminus. This is best visible for Gly29. The N-terminal residue (His28) is not observable due to fast exchange with the solvent.

Figure S6. pH dependent binding to chitin. Binding of 5.3 μ M CBP21 to 10 mg/ml β -chitin at pH ranging from 3 to 10. The degree of bound protein was estimated by measuring the fraction of unbound protein in the reaction supernatant after 3 h incubation at room temperature.

Figure S7. CBP21 purification. SDS-PAGE analysis of CBP21 purified by chitin affinity chromatography and eluted from the column material by 20 mM Tris-HCl, pH 8.0 and 0.2 M EDTA (lane 2) or 20 mM acetic acid (lane 3). The BenchMark protein ladder (Invitrogen) is shown in lane 1.

SI Table Legends

Table S1. Statistics for NMR structure determination.

SI References

1. Vaaje-Kolstad G, Houston DR, Riemen AHK, Eijsink VGH, & van Aalten DMF (2005) Crystal structure and binding properties of the *Serratia marcescens* chitin-binding protein CBP21. *J Biol Chem* 280:11313-11319.
2. Aachmann FL, Eijsink VGH, & Vaaje-Kolstad G (2011) H-1, C-13, N-15 resonance assignment of the chitin-binding protein CBP21 from *Serratia marcescens*. *Biomol NMR Assign* 5:117-119.
3. Keller R (2005) Optimizing the process of nuclear magnetic resonance spectrum analysis and computer aided resonance assignment. Ph.D (ETH, Zürich).
4. Farrow NA, *et al.* (1994) Backbone dynamics of a free and phosphopeptide-complexed Src homology 2 domain studied by ¹⁵N NMR relaxation. *Biochemistry* 33:5984-6003.
5. Kay LE, Torchia DA, & Bax A (1989) Backbone dynamics of proteins as studied by ¹⁵N inverse detected heteronuclear NMR spectroscopy: application to staphylococcal nuclease. *Biochemistry* 28:8972-8979.
6. Güntert P, Braun W, & Wüthrich K (1991) Efficient computation of 3-dimensional protein structures in solution from Nuclear-Magnetic-Resonance data using the program Diana and the supporting programs Caliba, Habas and Glomsa. *J Mol Biol* 217:517-530.
7. Shen Y, Delaglio F, Cornilescu G, & Bax A (2009) TALOS+: a hybrid method for predicting protein backbone torsion angles from NMR chemical shifts. *J Biomol NMR* 44:213-223.
8. Krieger E, Koraimann G, & Vriend G (2002) Increasing the precision of comparative models with YASARA NOVA - a self-parameterizing force field. *Proteins* 47:393-402.
9. Essmann U, *et al.* (1995) A Smooth Particle Mesh Ewald Method. *J Chem Phys* 103:8577-8593.
10. Krieger E, *et al.* (2009) Improving physical realism, stereochemistry, and side-chain accuracy in homology modeling: Four approaches that performed well in CASP8. *Proteins* 77:114-122.
11. Sorlie M, Seefeldt LC, & Parker VD (2000) Use of stopped-flow spectrophotometry to establish midpoint potentials for redox proteins. *Anal Biochem* 287:118-125.
12. Liu Y, Seefeldt LC, & Parker VD (1997) Entropies of redox reactions between proteins and mediators: the temperature dependence of reversible electrode potentials in aqueous buffers. *Anal Biochem* 250:196-202.
13. Wüthrich K (1986) *NMR of proteins and nucleic acids* (John Wiley & Son, Inc.).
14. Fan Y, Saito T, & Isogai A (2008) Preparation of chitin nanofibers from squid pen beta-chitin by simple mechanical treatment under acid conditions. *Biomacromolecules* 9:1919-1923.
15. Vaaje-Kolstad G, *et al.* (2010) An oxidative enzyme boosting the enzymatic conversion of recalcitrant polysaccharides. *Science* 330:219-222.
16. Wiseman T, Williston S, Brandts JF, & Lin LN (1989) Rapid measurement of binding constants and heats of binding using a new titration calorimeter. *Anal Biochem* 179:131-137.

Table S1.

| Input data for the structure calculation | |
|--|--------------|
| Total number of NOE distance constraints | 4330 |
| Intra | 2609 |
| Short | 781 |
| Medium | 250 |
| Long | 690 |
| Torsion angle constraints ^a | 231 |
| Structure statistics, 20 Conformers^b | |
| CYANA target function value (Å ²) ^c | 3.47 ± 0.53 |
| Maximum residual distance constraint violation (Å) | 0.33 ± 0.08 |
| Torsion angle constraint violations | |
| Maximum (°) | 4.00 ± 1.27 |
| Force field energies (kJ·mol⁻¹) | |
| Total | -54021 ± 102 |
| van der Waals | -1459 ± 21 |
| Electrostatic | -11801 ± 159 |
| PROCHECK Ramachandran plot analysis | |
| Residues in favored regions (%) | 87.2 |
| Residues in additionally allowed regions (%) | 12.2 |
| Residues in generously allowed regions (%) | 0.6 |
| Residues in disallowed regions (%) | 0.0 |
| RMSD to the average coordinates (Å)^d | |
| N, C ^α , C' | 0.25 |
| N, C ^α , C' (secondary structure) ^e | 0.21 |
| Heavy atoms | 0.34 |
| Heavy atoms (secondary structure) ^e | 0.30 |

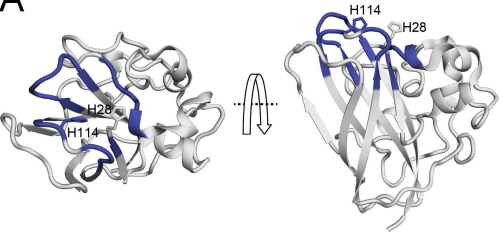
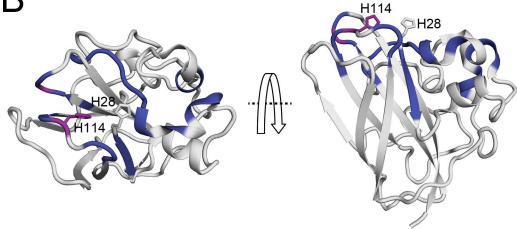
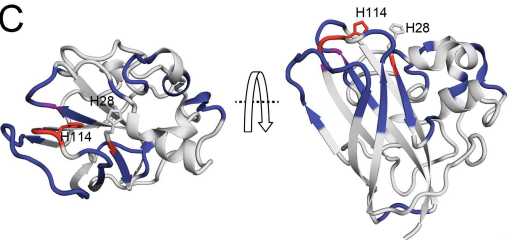
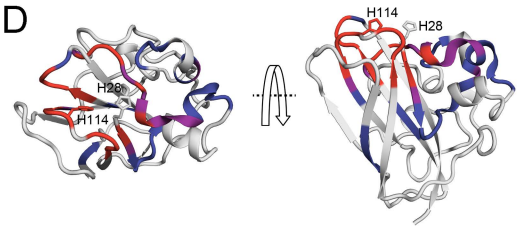
^a Obtained from secondary chemical shifts using the program TALOS+ (8).

^b The values given are the average and standard deviation over the 20 energy-minimised conformers with the lowest CYANA (Ver. 3.1) target function values, from which the NMR solution structure was derived.

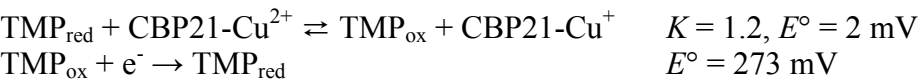
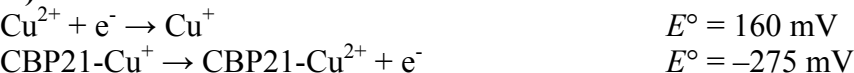
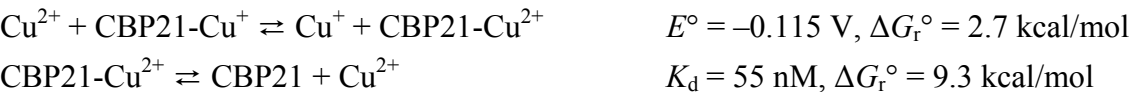
^c The average target function values for the 20 best CYANA conformers before energy minimisation.

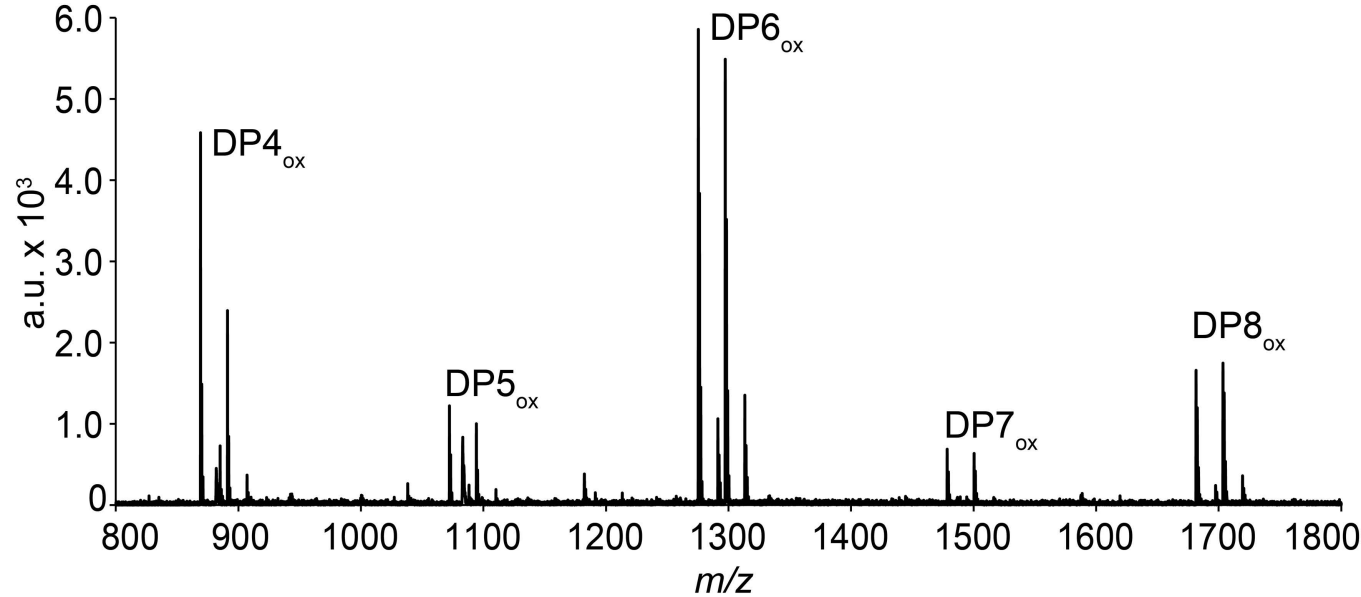
^d Average coordinates of 20 energy-refined conformers after superposition for best fit of the N, C^α, and C' atoms of the residues.

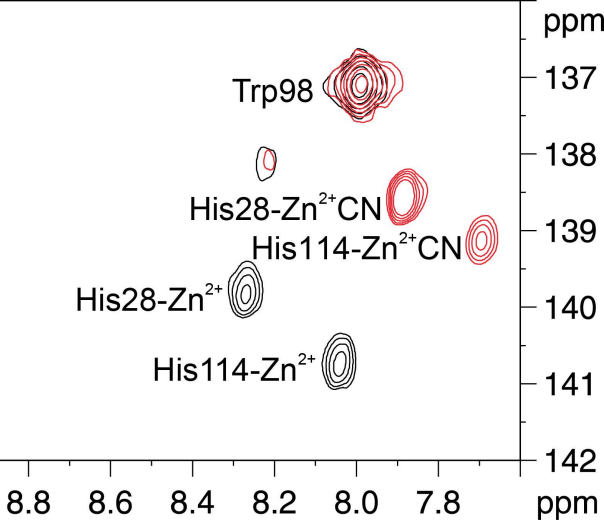
^e Residues 29-33, 37-44, 50-53, 56-58, 81-87, 97-110, 116-124, 136-140, 145-149, 157-164, 170-180, 185-196.

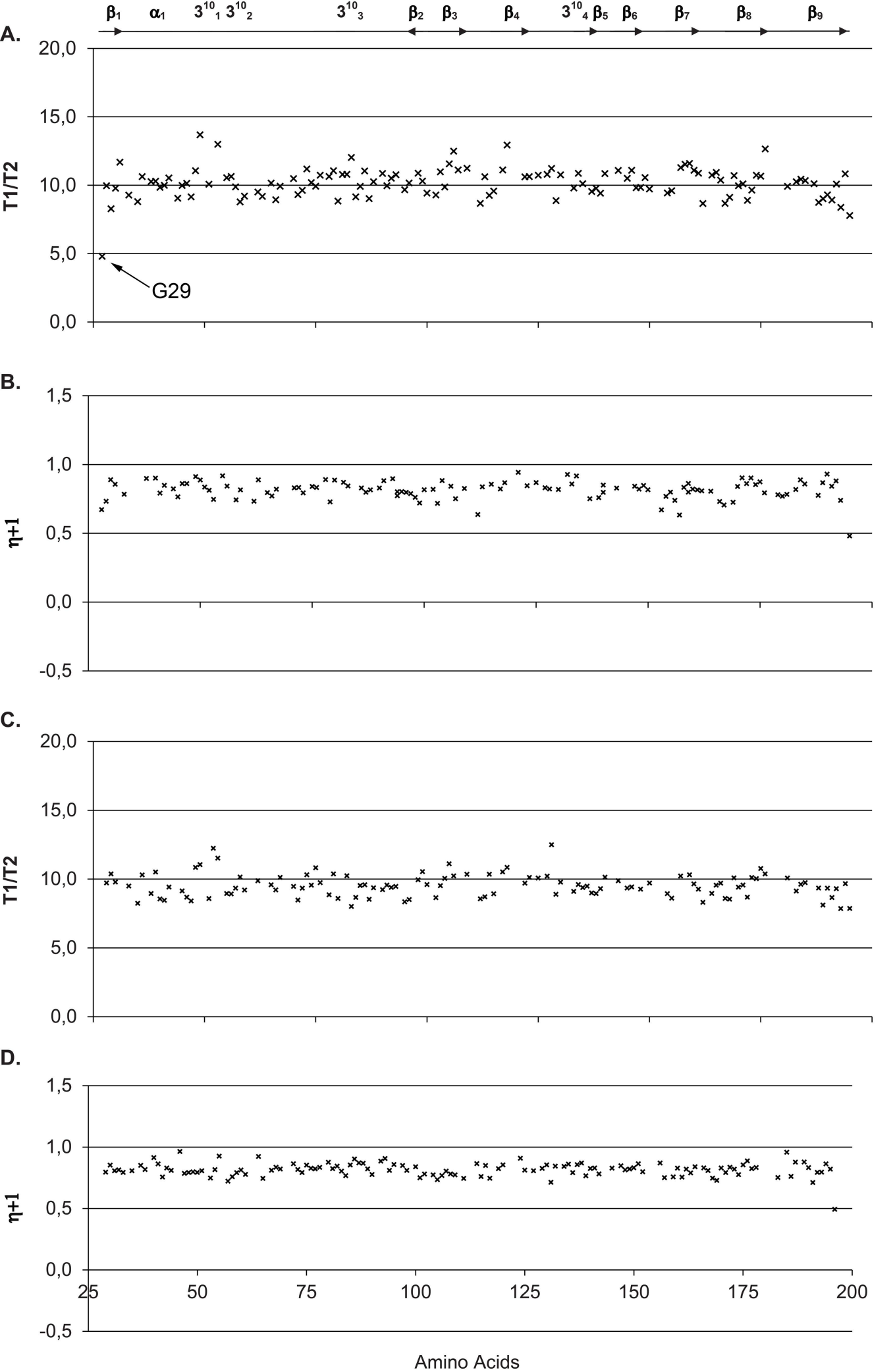
A**B****C****D**

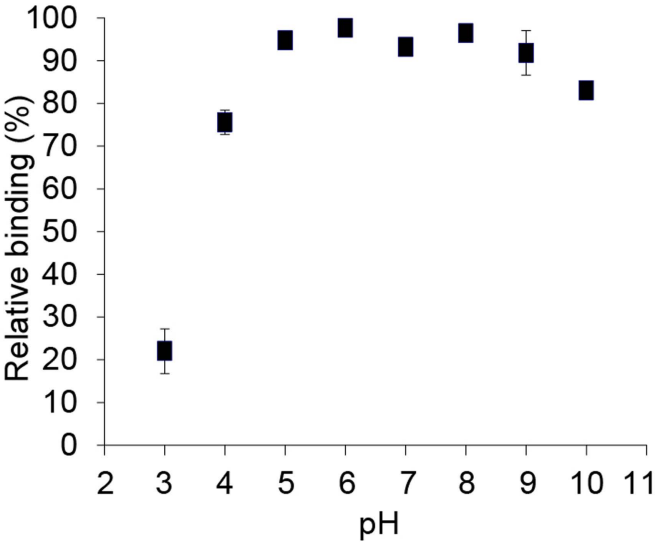
■ 10-100Hz
■ 100-200Hz
■ >200Hz

I)**II)****III)**









MW
(kDa)

1

2

3

50

20

CBP21

